

Unveiling ECRAM switching mechanisms using variable temperature Hall measurements for accelerated AI computation

Received: 30 April 2024

Accepted: 10 March 2025

Published online: 19 March 2025

 Check for updates

Hyunjeong Kwak¹, Junyoung Choi¹, Seungmin Han¹, Eun Ho Kim¹, Chaeyoun Kim², Paul Solomon³, Junyong Lee¹, Doyoon Kim¹, Byungha Shin², Donghwa Lee¹, Oki Gunawan³✉ & Seyoung Kim¹✉

Electrochemical random-access memory devices are promising for analog cross-point array-based artificial intelligence accelerators due to their high stability and programmability. However, understanding their switching mechanism is challenging due to complex multilayer structures and the high resistivity of oxide materials. Here, we fabricate multi-terminal Hall-bar devices and conduct alternating current magnetic parallel dipole line Hall measurements to extract transport parameters. Through variable-temperature Hall measurements, we determine the oxygen donor level at approximately 0.1 eV in tungsten oxide and reveal that conductance potentiation even at low temperatures results from increased mobility and carrier density. This behavior is linked to reversible electronic and atomic structure changes, supported by density functional theory calculations. Our findings enhance the understanding of electrochemical random-access memory switching mechanisms and provide insights for improving high-performance, energy-efficient artificial intelligence computation in analog hardware.

Deep neural network technology, commonly known as deep learning, has achieved a series of breakthroughs in AI capabilities^{1,2}. These models progressively improve their ability to solve complex problems by learning from data³. Further propelled by advances in algorithms, improved hardware platforms, and extensive datasets, AI now facilitates a range of functions including automation, content generation, and predictive maintenance across numerous sectors⁴. As the demand for computational power surges to support the expanding scope of AI applications, both specialized and conventional hardware developments are advancing to manage the billions of parameters and simple but data-intensive and repetitive computations required. In response to these growing demands, analog AI computation architectures using

cross-point arrays of non-volatile memory (NVM) devices have been proposed, promising significant increases in processing speeds and energy efficiency, thereby reducing time and energy costs⁵.

Analog AI computation involves physically executing vector-matrix multiplication in deep learning by arranging tunable conductive NVM in a cross-point array architecture. This approach minimizes the need for data transfer between memory and processor units and performs massively parallel computation in analog, enabling large computation acceleration while consuming less energy⁶. However, realizing this concept demands prioritizing the selection of appropriate NVM candidates. Furthermore, manipulating numerical values in the format of analog physical quantities

¹Department of Materials Science and Engineering, Pohang University of Science and Technology, Pohang, South Korea. ²Department of Materials Science and Engineering, Korea Advanced Institute of Science and Technology, Daejeon, South Korea. ³IBM T. J. Watson Research Center, Yorktown Heights, NY, USA. ✉e-mail: ogunawa@us.ibm.com; kimseyoung@postech.ac.kr

poses a challenge. In particular, if the vulnerability to variation and noise in analog signals remains unresolved, the advantage of analog AI computation will ultimately be limited to the application working with limited accuracies such as approximation^{7,8}.

Electrochemical random-access memory (ECRAM) stands as a promising cross-point element for performing analog AI computation. With a transistor-like three-terminal structure, ECRAM's channel conductance can be modulated by applied gate bias which induces ion migration into or out of the channel material^{9,10}. In contrast to two terminal counterparts, the device structure with the third terminal separates the read and write pathways to provide improved controllability and ease for device optimization. Such devices based on the electrochemical movement of ions offer excellent programmability and broaden versatility with multilevel, low cycle-to-cycle, and device-to-device variation. Among various ions considered, oxygen ion-based ECRAM (O-ECRAM) devices have attracted many researchers due to their excellent programmability and foundry-friendly material compositions. Transition metal oxide materials such as WO_3 ^{11,12}, $\text{Pr}_{1-x}\text{Ca}_x\text{MnO}_3$ ¹³, TiO_2 ¹⁴, and MoO_3 ^{15,16} have been considered as channel layers for O-ECRAM. Recently, various reports have highlighted ECRAM-based cross-point array architecture¹⁷ including in-situ training^{18,19}, demonstrating excellent switching characteristics²⁰.

Understanding and tracking the changes in materials within a device is essential. To advance towards a technology specialized in analog AI computation with high energy efficiency and training capabilities, insight from fundamental studies on atomic and electronic behavior of materials during the switching process of ECRAM are necessary to enable appropriate material selection and optimization. Although numerous studies have investigated how electrochemical reactions and ion diffusion underlie various switching mechanisms in resistive random-access memory (ReRAM) and other memory devices, these mechanisms are not necessarily identical to those in ECRAM. For example, filamentary-based processes (e.g., electrochemical metallization, valence change mechanism, thermochemical mechanism) rely on localized conduction paths and Joule heating²¹, whereas ECRAM exhibits a bulk switching mechanism driven by electrochemical redox reactions in the channel and electrolyte, along with the electric double layer (EDL) effect and electrochemical doping²². Nevertheless, the underlying mechanisms responsible for the switching characteristics of ECRAM remain to be revealed. This deficiency can be attributed to three primary factors: the challenge of observing oxygen vacancies or oxygen ion migration, the intricate multilayer structure of ECRAM, and the intermixing of the conduction and switching mechanisms resulting from the separation of read/write pathways. Therefore, advanced measurement techniques with high-sensitivity is required to shed light on revealing the switching mechanism in ECRAM.

In this work, we develop ECRAM Hall-bar devices using WO_{3-x} as the channel material to explore their essential transport properties, including carrier type, mobility, carrier density, and operational principles. Our method, leveraging an AC magnetic parallel dipole line (PDL) Hall system, overcomes a longstanding measurement barrier that was previously nearly impossible to address for high-resistance channels. Specifically, we perform Hall measurements by applying a time-varying magnetic field and a lock-in technique, which allows for the detection of weak Hall signals in WO_{3-x} channels, effectively eliminating DC background and noise^{23–25}. Furthermore, we conduct the comparative study on resistive switching in ECRAM devices at low temperatures, capturing crucial physical parameters through Hall measurements at various conductance states. By employing first-principle calculations, we quantitatively analyze the observed physical properties, providing insights into optimizing ECRAM performance for use as an analog AI computation accelerator. Building on these insights, we assess the robust cycle-to-cycle performance of ECRAM and investigate its potential impact on the training of neural networks.

Results

Device configuration and switching behavior

The operational principles of ECRAM and a cross-point array-based AI accelerator chip designed for brain-like efficiency and functionality²⁶ are illustrated in Fig. 1a. This neuromorphic computing system integrates an analog AI accelerator, with the cross-point array centrally positioned for pivotal computational acceleration. ECRAM's key function is its capability to store analog conductance values, which depends on the ion concentration in the transition metal oxide channels and perform computations. Specifically, we use WO_{3-x} , where a reduction in oxygen ions increases the channel conductance—known as potentiation. Conversely, an increase in oxygen ions decreases conductivity, a phenomenon referred to as depression.

Hall measurement is a powerful approach for revealing fundamental operating mechanisms of ECRAM. To facilitate these measurements, we converted the conventional three-terminal ECRAM structure into a Hall-bar configuration, as illustrated in Fig. 1b. This configuration allows to measure longitudinal resistance (R_{xx}) and transverse magnetoresistance (R_{xy}) at finite magnetic fields by flowing a current through the Hall bar and measure the voltage drop between the corresponding terminals. The sheet resistance is calculated using the formula $R_s = R_{xx} \times \frac{W}{L}$, where W is the width and L the length of the channel. The channel conductivity is defined as $\sigma = \frac{1}{R_s d}$, where d is the film thickness. We fabricate an additional gate terminal to apply a gate voltage, V_{write} , and monitor change in the Hall signal of the channel material during switching. The inset of Fig. 1b shows an optical micrograph of a fabricated ECRAM Hall-bar device with 10 terminals. The transmission electron microscope (TEM) image in Fig. 1c reveals the material stack of the device: a WO_{3-x} channel, HfO_2 as the electrolyte layer, and W as the gate electrode.

In Fig. 1d, we applied 100 voltage pulses with +4.0 V amplitude and 0.5 s pulse width for potentiation and 100 voltage pulses with −4.0 V amplitude and 0.5 s pulse width for depression, and displayed the conductance as a function of pulse number at $V_{\text{read}} = 0.01 \text{ V}$. We observe the multi-level switching operation and switching window of the device. As a three-terminal device, ECRAM operates vertically, allowing ion migration into or out of the channel (write), while the conductance value can be read horizontally through source and drain (read). When a positive voltage is applied to a WO_{3-x} channel-based ECRAM device, oxygen ions penetrate from the channel to the gate, increasing conductivity. A negative voltage, on the other hand, causes ion migration to reverse, resulting in a decrease in conductivity.

Channel conduction mechanism

The Hall effect, discovered in 1880, has been an important tool for assessing semiconductor materials, providing information on carrier type, mobility and carrier density²⁷. However, accurate Hall measurement was not possible for low mobility and/or high-resistance materials by conventional DC Hall measurement setup. We overcome this issue by using two rotating cylindrical DC magnets as shown in Fig. 2a, and placing the ECRAM Hall-bar device between the magnets to apply the strong AC magnetic field up to 2 T. The Hall signal is enhanced and stabilized by the reinforced magnetic field, enabling measurements with samples with low resistivity (Supplementary Fig. 1). Furthermore, the PDL measurement system is configured within a cryostat to enable Hall measurements at low temperatures. As indicated by the arrows in Fig. 2a, we conducted Hall measurements at temperatures ranging from 300 K to 50 K with 10 K intervals to confirm the conduction mechanism of the WO_{3-x} channel material. For precise temperature control, we used three temperature sensors to accurately monitor the sample temperature (Supplementary Fig. 2).

Figure 2a also illustrates the use of Fourier transformation (FT) to convert the Hall coefficient into a frequency signal, transforming Hall resistance into a frequency output (Supplementary Fig. 3). The FT isolates the amplitude associated with the Hall signal, while the power

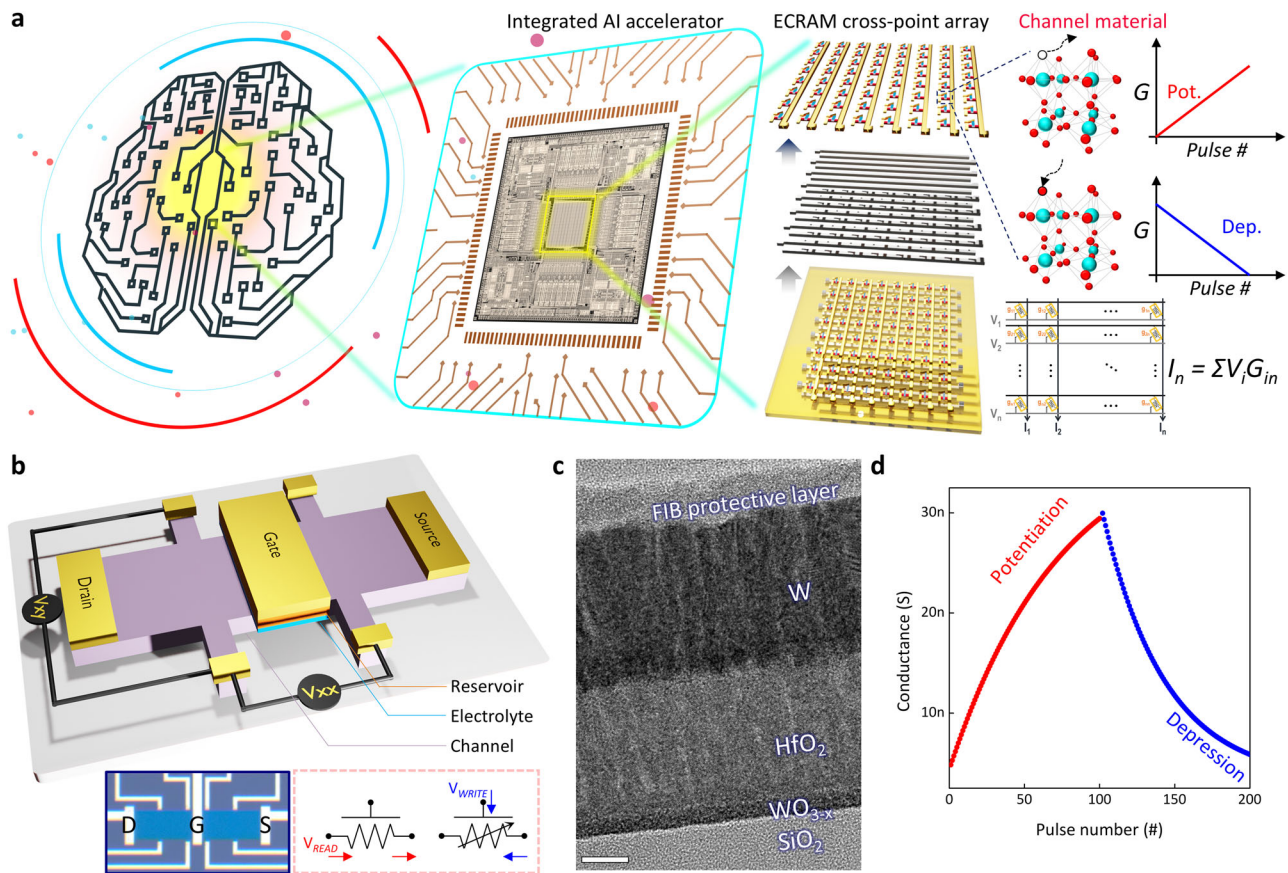


Fig. 1 | Analog AI hardware based on ECRAM technology and ECRAM Hall bar device. **a** Illustration of ECRAM technology for AI computation aiming for brain-like efficiency and functionality. ECRAM, emulating synaptic devices within the cross-point array, exhibits resistive switching based on ion migration. **b** ECRAM Hall-bar structure and operation methods. The gate stack of ECRAM is made up of three layers; channel, electrolyte and reservoir. ECRAM has three terminals, allowing read

operation through source and drain, and write operation through gate and channel. The inset OM image depicts 11 terminals, with additional terminals fabricated between the region adjacent to the gate and the region within the channel for comparative analysis. **c** Transmission electron microscope image of the device cross-section. (Scale bar: 10 nm) **d** Conductance modulation in a ECRAM device by applying 100 potentiation and 100 depression pulses.

spectral density enhances periodic signals, thereby confirming signal quality. The lock-in amplifier output values, derived through FT (in-phase and out-of-phase components), help eliminate background noise and drift, isolating Hall resistance induced by the magnetic field.

To accurately characterize the properties of ECRAM device, we try to understand the conduction mechanism of the channel material. WO_{3-x}, which is commonly used as an oxide channel material in ECRAM, is a transition metal oxide with a wide band gap ranging from 2.6 to 3.0 eV^{28,29}. It is a viable contender for neuromorphic applications because of its capacity to bridge the gap between metal and semiconductor states, which is determined by its oxygen content and stability. Hall-bar device with an active area of 60 × 20 μm² and a film thickness (*d*) of 4.5 nm was used in the measurement setup. Using radio frequency (RF) magnetron sputtering, ohmic contacts were deposited on the protrusions of 10 × 10 μm² WO_{3-x} thin films. These samples exhibit n-type characteristics and demonstrate strong temperature dependence.

Figure 2b illustrates that the resistivity of WO_{3-x} decreases as temperature increases, a behavior typical of semiconductor materials where thermal energy enables more electrons to move to the conduction band, reducing resistance. The relationship between resistivity and temperature adheres to the Mott variable range hopping (VRH) model:

$$J_{\text{VRH}} = \sigma_0 \exp\left(-\frac{T_0}{T}\right)^{\frac{1}{4}} \cdot E \quad (1)$$

where σ_0 is the electrical conductivity at temperature of T_0 ^{30,31}. This conduction mechanism is indicative of disordered systems with localized charge carriers, consistent with the properties of the amorphous WO_{3-x} thin films we studied³⁰. When analyzing the charge transport mechanism, we considered both small-polaron hopping (SPH) and VRH. Given the low-temperature range of our experiments ($T < 300$ K), we selected over SPH due to the lower activation energies requirements, which better aligns with the observed switching behavior. VRH, characterized by hopping between localized states, provided a superior fit to our experimental data, particularly in the 200–300 K range where switching occurs (Supplementary Fig. 4). Additionally, the carrier mobility, measured at approximately 50 cm² V⁻¹ s⁻¹, shows minimal variation but tends to fluctuate more at lower temperatures. This is likely due to changes in contact resistance at low temperatures, possibly arising from alterations in metal contact resistance or at the wire bonding area. Moreover, Hall measurements with independent WO_{3-x} channel material without the gate stack showed no significant mobility changes with temperature (Supplementary Fig. 5).

The carrier density decreases sharply with temperature, as shown in Fig. 2c. This indicates that the material operates in the freeze-out regime³², where carrier density increases as electrons transition to the conduction band with increasing temperature. An Arrhenius plot, relating the change in carrier density with temperature, helped calculate the activation energy (shallow donor level) at about 98.9 meV. This aligns with the reported shallow level of oxygen vacancies in WO₃,

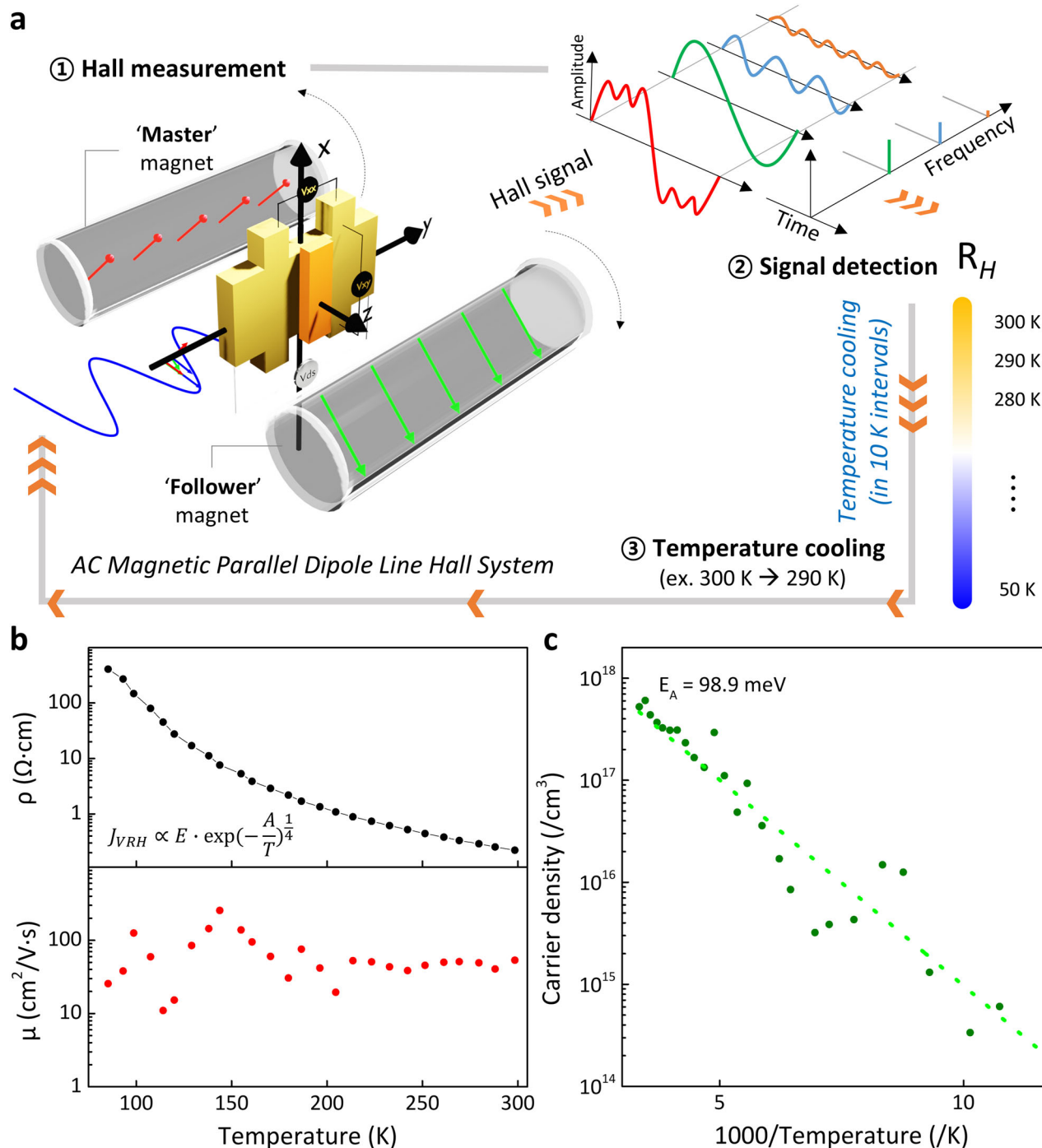


Fig. 2 | ECRAM Hall measurement results at 50 K to 300 K without resistive switching. **a** Illustration of the temperature-dependent PDL Hall measurement procedure without resistive switching (V_g is grounded). This measurement process is repeated at 10 K intervals while lowering the temperature, ranging from 300 K down to 50 K, to measure carrier type, density, and mobility values. **b** ECRAM resistivity (ρ) and carrier mobility (μ) extracted from the measured R_{xx} and R_{xy}

value. The temperature dependence of WO_{3-x} resistivity exhibits semiconductor behavior, while the carrier mobility follows a lognormal distribution and maintains a value of approximately $50 \text{ cm}^2\text{V}^{-1}\text{s}^{-1}$. **c** Activation energy extraction through Arrhenius plot analysis. The carrier density increases as the temperature rises, indicating a freeze-out regime. The activation energy is estimated to be 98.9 meV.

ranging from 0.1 to 0.5 eV³³, as confirmed by both experimental and theoretical studies on WO_3 .

Switching behavior at room temperature

The switching mechanism of the ECRAM device is articulated through three steps: (1) ion migration within the electrolyte, (2) ion diffusion into the channel, and (3) electrochemical reactions³⁴. Upon application of a gate voltage, oxygen ions (or oxygen vacancies) migrate from the

electrolyte toward the channel, accumulating at the interface before diffusing into the channel. This migration requires electrons to maintain charge neutrality, which are provided by the $\text{W } 5d$ orbital, associated with the conduction band of n-type WO_{3-x} , thereby increasing the channel's conductance. This process results in reversible oxygen ion (oxygen vacancy) doping through the gate voltage, leading to analog changes in the conductance of the WO_{3-x} channel. The transfer curve provides insights into the underlying switching mechanism of

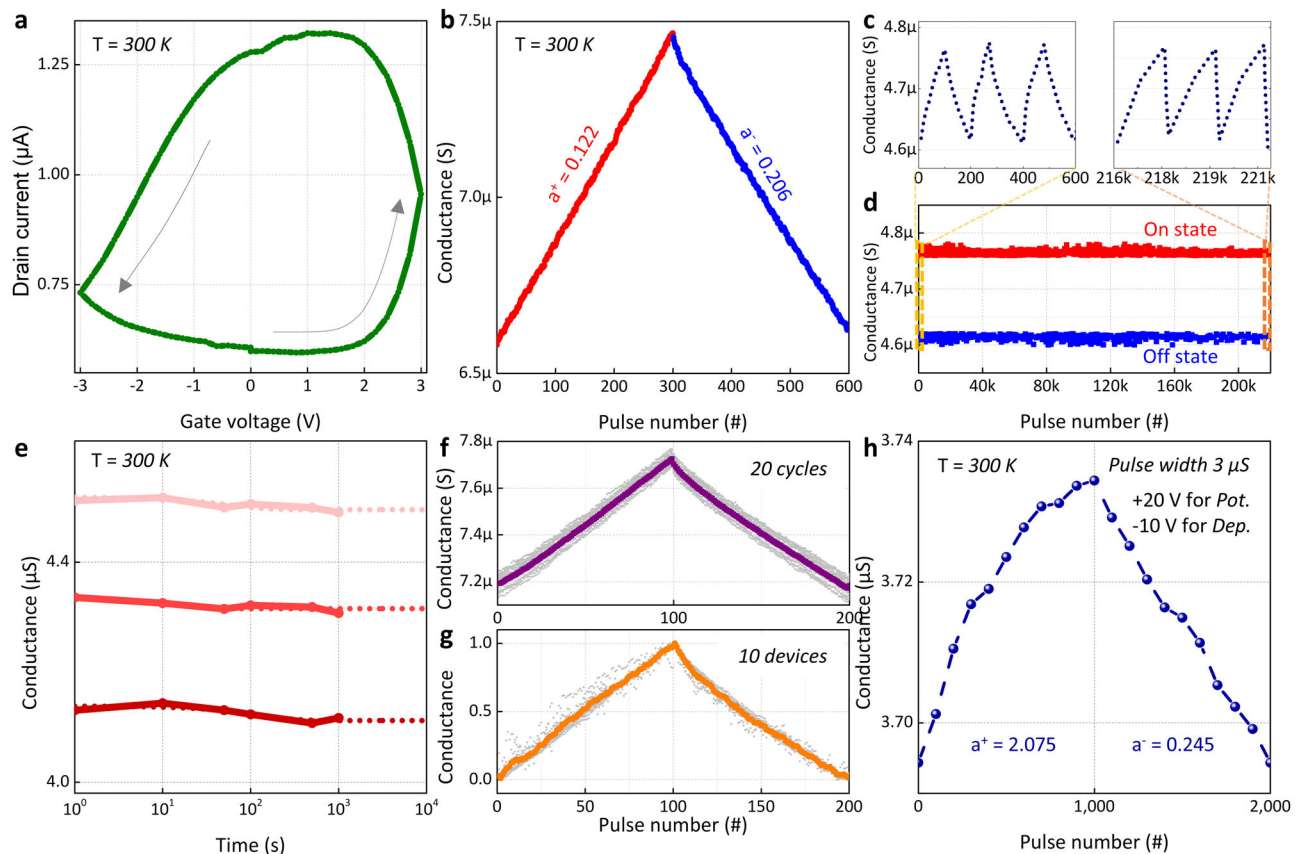


Fig. 3 | Switching and retention behavior at room temperature. **a** Transfer curve of the WO_{3-x} ECRAM by sweeping gate voltage from 0 to +3 V, then to -3 V, and back to 0 V in one cycle to examine memory window. **b** Pulsed conductance modulation measurement with 300 up pulses at +1.5 V and 300 down pulses at -0.8 V, using a pulse width of 0.5 s. **c**, **d** Endurance characteristics over 200,000 write pulses with a pulse width of 50 ms, applying +5 V for 100 up pulses and -1.5 V for 100 down pulses. **e** The retention characteristics at 300 K over a duration of 3 h for four different states. The retention time, defined as the time required for the

conductance to decrease by up to 2%, shows minimal change over the 3-h period. **f** Cycle-to-cycle variations over 20 cycles of 100 up and 100 down pulses on the same device. V_{write} is +1.5 V for up pulses and -0.8 V for down pulses with a pulse width of 0.5 s. **g** Device-to-device variations for devices with the same dimension. Normalized conductance graph of 10 devices. **h** Switching speed by applying consecutive 1000 up and 1000 down pulses. 3 μs pulse width is used, and the linearity is calculated as 2.075 during potentiation (a^+) and 0.245 during depression (a^-).

the device. As gate voltage increases from 0 to a positive gate bias, the drain current, I_d , correspondingly increases, which can be attributed to the formation of an EDL and the subsequent doping of the channel with oxygen vacancies. The EDL effectively modulates the channel conductance by creating an accumulation of charge carriers at the electrolyte/channel interface, facilitating the increase in I_d . Conversely, as gate voltage is reduced from +V back to 0, I_d diminishes due to the disappearance of the EDL and the partial migration of oxygen vacancies back to their initial positions. This reversible process is indicative of the dynamic interaction between the ionic species within the electrolyte and the channel material, which governs the conductance state of the device^{35,36}. Figure 3a displays the transfer curve (measured at $V_{\text{ds}} = 0.1$ V), where the counterclockwise hysteresis exhibits the non-volatile reversible nature of oxygen ion (oxygen vacancy) doping. The counterclockwise direction of the loop signifies that the device retains its doped state even after the gate voltage is removed, underscoring the stability of the switched state. Furthermore, the gradual return of I_d to its original state as the gate voltage is reduced highlights the controlled and stable nature of ionic migration within the system. These results demonstrate the reliable and reversible switching of the ECRAM device through ion modulation, as directly reflected in the transfer curve, which captures the ion migration inherent in the oxygen vacancy dynamics.

Figure 3b shows the device's switching behavior with 300 repetitive potentiation and depression pulses, each with a pulse width of

500 ms. The changes in oxygen content between the on and off states of the device were confirmed through TEM images (Supplementary Fig. 6), supporting the switching mechanism. Linearity remains consistently stable over 600 pulses, achieving values of 0.122 during potentiation and 0.206 during depression, as derived from the behavior model used in the NeuroSim architecture³⁷. As shown in Supplementary Fig. 7, repeating this measurement for 60 cycles yielded near-perfect linearity throughout, confirming the robustness of the device switching characteristics.

The endurance of the device over 200,000 pulses is shown in the graph, depicting the pulse responses for each cycle, as illustrated in Fig. 3c, d. The test was conducted with +5 V and -1.5 V write voltage, each 50 ms in pulse duration, and the device exhibited consistent switching behavior throughout the entire pulse sequence. Notably, the switching performance showed minimal variation, indicating strong reliability in the device operation. The endurance test results indicate stable performance up to 221,000 pulses, after which the device continued to operate but began to exhibit signs of degradation.

Given that changes in state can induce variations in electrical parameters during Hall measurements, having a device with robust retention characteristics was critical. Thus, the device was optimized to ensure enhanced retention performance, maximizing the accuracy and reliability of Hall results at 300 K. The retention characteristics of the device over a 3-h (10,800 s) period are plotted in Fig. 3e, showing data for three distinct programming states. Retention time is defined

as the duration required for the conductance to decrease by 2%. At room temperature, the retention time for the lowest conductance, when extrapolated, was estimated to exceed 10^9 seconds (more than 10 years), while minimal variation was observed, making it difficult to determine a specific retention time.

In Fig. 3f, g, the cycle-to-cycle and device-to-device variations are analyzed to assess the reliability and uniformity of the ECRAM device switching behavior in analog AI hardware. The top graph shows the overlaid results of 20 successive cycles, demonstrating repeatable conductance modulation with minimal variation between cycles. The average and standard variation of the conductance values were calculated for each cycle, with the largest standard deviation observed at pulse number 187, where the average conductance was 7.22 μ S, and the standard deviation was 35.9 nS. This consistency across cycles highlights the stability of the device switching performance. The bottom graph presents the device-to-device variation, where the conductance values of 10 different devices were normalized and superimposed. After normalization, the mean conductance was 0.089, and the standard deviation, calculated in the section with the largest difference, was 100.3% of the mean. While some variability between devices exists, the overall trend remains consistent, indicating that the device-to-device variation falls within the acceptable limits for reliable operation in analog AI hardware³⁸.

The retention-optimized device demonstrates a switching speed, achieving a pulse width of 3 μ s, as shown in Fig. 3h. The switching behavior shows both symmetry and linearity, with a linearity value of 2.075 for potentiation and 0.245 for depression, ensuring consistent performance across multiple states. Additionally, the energy consumption per pulse has been calculated at 9.81 fJ for potentiation and 5.46 fJ for depression, highlighting the energy efficiency. Although the switching speed is currently limited by the structural constraints of the Hall-bar configuration, further improvements can be achieved by reducing ion migration distance and increasing migration speed through device scaling and material optimization.

Channel modulation mechanism

In this study, we present variable-temperature Hall measurement results on ECRAM devices with a gate terminal. This approach incorporates three principal components: a high-sensitivity Hall measurement with an AC magnetic PDL Hall system, temperature-dependent measurement capability, and the application of a gate voltage to monitor the channel conductance modulation. To investigate the temperature-dependent conductance modulation mechanism, we conducted measurements as shown in Fig. 4a. Initially, at room temperature, we applied ± 2.0 V for 80 pulses each of potentiation and depression to confirm the device's resistive switching behavior. These pulse conditions were chosen to achieve a high on/off ratio for clear observation of changes in Hall parameters, rather than to maximize linearity. Previous work has shown that the device maximum conductance can be estimated from its sheet resistance and area³⁹. For the device used in the Hall measurements, this calculation yielded a maximum conductance of 43.2 nS. Given the practical limitations of Hall measurements and the risk of device damage from excessive voltages, the on-state was defined as any conductance within 10% of this calculated maximum, and pulses of 2 s were applied incrementally until the on-state was reached. Retention was then evaluated for 300 s after every 20 pulses to confirm that the Hall measurements could be carried out consistently, without unintended changes in the on/off states.

For the off-state Hall measurements, -2.0 V was applied for 80 depression pulses to reduce the device conductance, immediately followed by a Hall measurement. The device was then driven back to the on-state by applying $+2.0$ V for 80 potentiation pulses, after which another Hall measurement was taken. In all cases, a channel read voltage of 0.1 V was used, determined from post-fabrication I - V

measurements that confirmed the ohmic region. These measurement sequences were repeated while lowering the temperature in 20 K increments to investigate any temperature-dependent changes in the ECRAM switching mechanism. In addition, contact resistance was continuously monitored throughout the Hall measurements (Supplementary Fig. 8) to ensure that it did not affect the observed results.

The switching results according to temperature are depicted in Fig. 4b. At room temperature, the on/off ratio is approximately 90, which decreases to 2.54 at 260 K and further to 1.31 at 240 K. This confirms the exponential dependence of ECRAM switching behavior on temperature, an observation detailed in Supplementary Fig. 9. Furthermore, we examined the retention characteristics of ECRAM at low temperatures as shown in Fig. 4c. The displayed retention data, derived not from the measurements in Fig. 4a but from settings where the device was programmed to 40 nS and the temperature subsequently lowered, show enhanced retention times at reduced temperatures. At 208 K (with set stage temperature of 200 K), the programmed value remained stable without any noticeable change over a 3-h duration (Supplementary Fig. 9).

To elucidate the switching mechanism further, we conducted sequences 3 and 4 from Fig. 4a, monitoring physical parameters that change as the device conductance modulates. We confirmed that gate current stayed negligibly small, ranging from sub- to tens-of-picoamperes, and by about 1000 times lower from the drain current, which were crucial for accurate measurement and analysis. Figure 4d illustrates changes in mobility and carrier density due to switching. From 260 K and 300 K, conductance increases from the Off state, through the intermediate (IMD) state, to the On state. Notably, mobility and carrier density increase by 18.9 and 2.5 times at 300 K, respectively. However, at 280 K, the rate of increase slows to 1.4 and 1.7 times. Furthermore, at 260 K, unlike at the higher temperature, as conductance increases, mobility rises to 1.78 times, but carrier density decreases to 0.66 times. These change at 260 K suggests that the electrochemical mechanism of ECRAM undergoes a shift around this temperature. The reversal in the behavior of mobility and carrier density as temperature decreases may be due to temperature-dependent ion dynamics. In contrast, at higher temperature ion migration and charge carrier transport become more efficient, leading to greater increases in both mobility and carrier density.

First-principles hybrid functional calculations with HSE06 formalism⁴⁰ are employed to understand variable-temperature Hall measurements results. Because amorphous WO_3 structure comprises same building blocks as the crystalline phase⁴¹, we use monoclinic WO_3 with $\text{P2}_1/\text{n}$, which is the most common structure in WO_3 . The unit cell of monoclinic WO_3 is shown in Fig. 5a. Since oxygen vacancy concentration increases exponentially with temperature⁴², we examine how vacancy concentration affects conductance of WO_3 channel. Previous studies report that oxygen vacancy with 2+ charge (V_O^{2+}) is the most stable charge state within the bandgap^{33,42}, so we consider only V_O^{2+} in our system. We determine the most energetically favored site of V_O^{2+} among three non-equivalent sites (s_x , s_y , s_z), shown in Fig. 5a. The calculation results show that site s_z , in which V_O^{2+} is parallel to the z -axis, has the lowest vacancy formation energy, consistent with previous study³³. In order to investigate the effect of V_O^{2+} on electronic structure of WO_3 , we prepare three distinct systems: a pristine vacancy-free system represented by WO_3 , low oxygen vacancy system denoted as $\text{WO}_{2.938}$ (one V_O^{2+} within a $1 \times 1 \times 2$ supercell), and high oxygen vacancy system designated as $\text{WO}_{2.875}$ (two V_O^{2+} aligned along z -axis within a $1 \times 1 \times 2$ supercell) (Supplementary Fig. 10). Our results show that the bandgap of WO_3 is 2.60 eV, which closely agrees with the experimental value of 2.62 eV⁴³. Upon removing oxygens, the bandgap exhibits a progressive reduction to 2.40 eV in $\text{WO}_{2.938}$ and further decreases to 2.30 eV in $\text{WO}_{2.875}$, as illustrated in Fig. 5b. To further investigate the relationship between V_O^{2+} and the bandgap, we conduct a comparative analysis of the band structures for three systems, see Fig. 5c. For

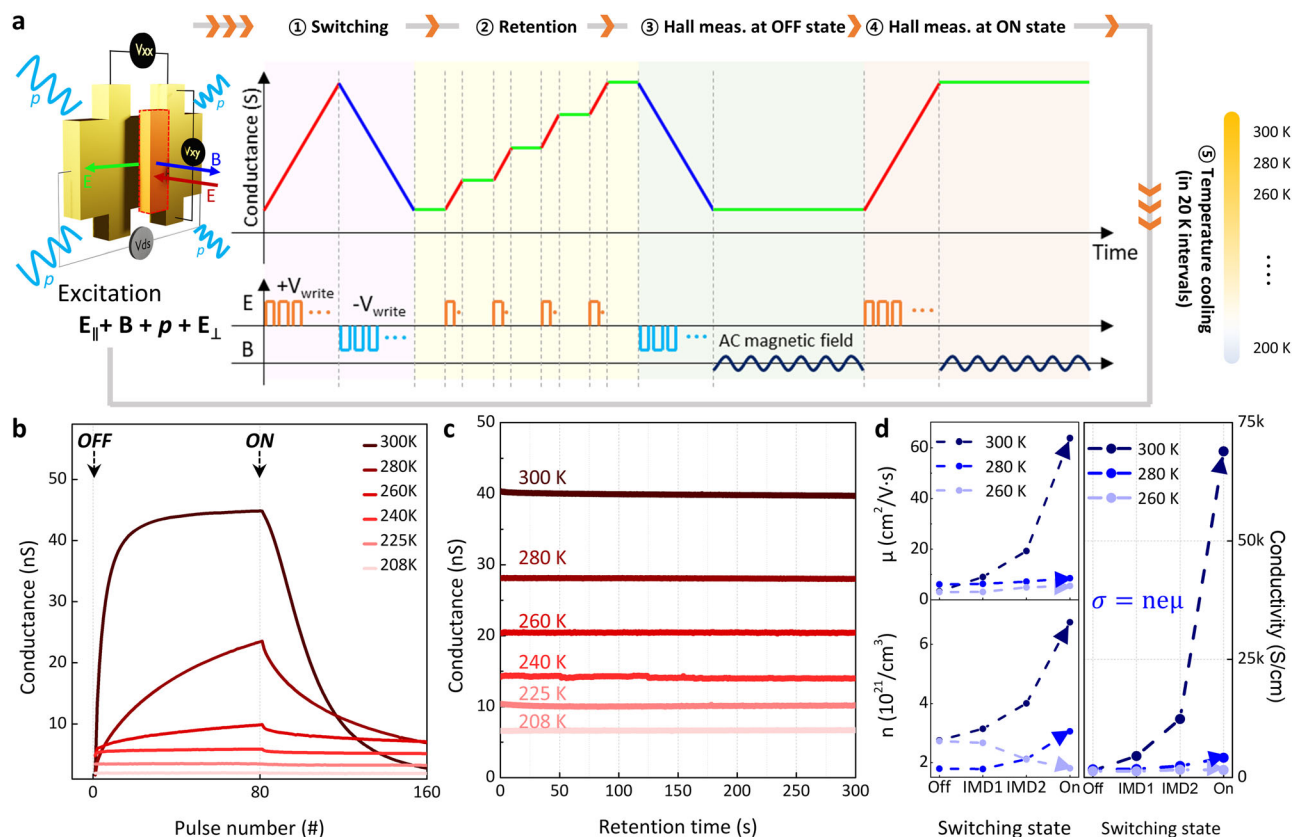


Fig. 4 | Variable-temperature ECRAM Hall measurement with resistive switching. **a** ECRAM Hall measurement setup and sequence at various temperatures with resistive switching. The retention characterization is checked to ensure stability during the Hall measurement duration. These measurements were repeated while decreasing the temperature from 300 K to 200 K in vacuum. **b** Switching characteristics of device at various temperatures. Different conductance state was obtained by write voltage of ± 2.0 V applied to the gate electrode with V_{ds} of 0.1 V.

The switching range sharply decreases as the temperature decreases. **c** Retention characteristics at various temperatures improve inversely as the temperature decreases. **d** Change of carrier mobility (μ) and carrier density (n) at 260 K, 280 K and 300 K between on, intermediate and off state. At 280–300 K, both carrier mobility and carrier density increase as the device conductivity increases. The magnitude of these changes decreases as the temperature decreases. The state and the direction of change marked in inset corresponds to the main figure.

$\text{WO}_{2.938}$, one $V_O^{\bullet\bullet}$ state (purple line) appears near the conduction band minimum (CBM). Similarly, two $V_O^{\bullet\bullet}$ states are observed near CBM in $\text{WO}_{2.875}$. It is obvious that the formation of $V_O^{\bullet\bullet}$ states near CBM yields the reduction of the bandgap, resulting in a gradual decrease with vacancy concentration. We further examine the spatial distribution of the newly generated states and confirm that the defect states are localized on W atoms near $V_O^{\bullet\bullet}$ (Supplementary Fig. 11). The localization of $V_O^{\bullet\bullet}$, in turn, induces a large extent of electron delocalization. As this delocalization expands, a large 2D polaron forms, which leads to high mobility^{44–46}. In conclusion, our calculation results demonstrate that the observed increase in conductivity with temperature is a result of the bandgap reduction induced by the formation of $V_O^{\bullet\bullet}$ states near CBM.

Impact of cycle-to-cycle variation on AI computation

Based on such topotactic changes, ECRAM devices have demonstrated low cycle-to-cycle variation, as extensively reported in previous studies^{19,47}. In many memory technologies, local conduction pathways or morphological changes can introduce variability over repeated operations^{48,49}; by contrast, the uniformity of ECRAM's topotactic transitions help maintain stable performance across cycles. Within the same device configuration where Hall measurements were taken—specifically, devices with a gate width of 4 μm and channel length of 25 μm —cycle-to-cycle variation exhibited minimal deviation, as shown in Supplementary Fig. 12. To assess the impact of cycle-to-cycle variation on neural network training, we conducted experiments using a stochastic gradient descent (SGD) algorithm to

train a multi-layer perceptron, simulating pattern recognition accuracy with the MNIST dataset. These tests revealed that recognition accuracy tended to increase as the variation decreased. Our devices showed a cycle-to-cycle variation of only 1.2%, achieving a test accuracy of over 97.8% (Supplementary Fig. 12), which is within 0.2% from the software-level accuracy, 98%. Therefore, the stability of our device's operation makes it highly suitable for AI computation requiring high accuracy.

In summary, we fabricated a multi-terminal ECRAM Hall-bar device and performed high-sensitivity PDL Hall measurement to elucidate its conduction and switching mechanism. The temperature-dependent conductance measurement revealed semiconductor behavior that showed decreased conductance as temperature decreases, indicative of a Mott VRH relationship. Electron mobility in the ECRAM channel layer showed little temperature dependence and remained constant at approximately $50 \text{ cm}^2 \text{V}^{-1} \text{s}^{-1}$. Through Arrhenius plot analysis, we confirmed an activation energy closely matching the predicted oxygen donor level of WO_{3-x} reported in the literature at 0.1 eV. We observed the switching characteristics of the ECRAM devices at room temperature and confirmed that specifications such as linearity, symmetry, endurance and cycle-to-cycle and device-to-device variation exceeded the requirements for AI computing. We further evaluated the switching and retention characteristics of ECRAM at low temperatures, revealing lower conductance modulation and longer retention at reduced temperatures. We also monitored changes in physical parameters during ECRAM switching through variable-temperature Hall measurements. A key finding was that

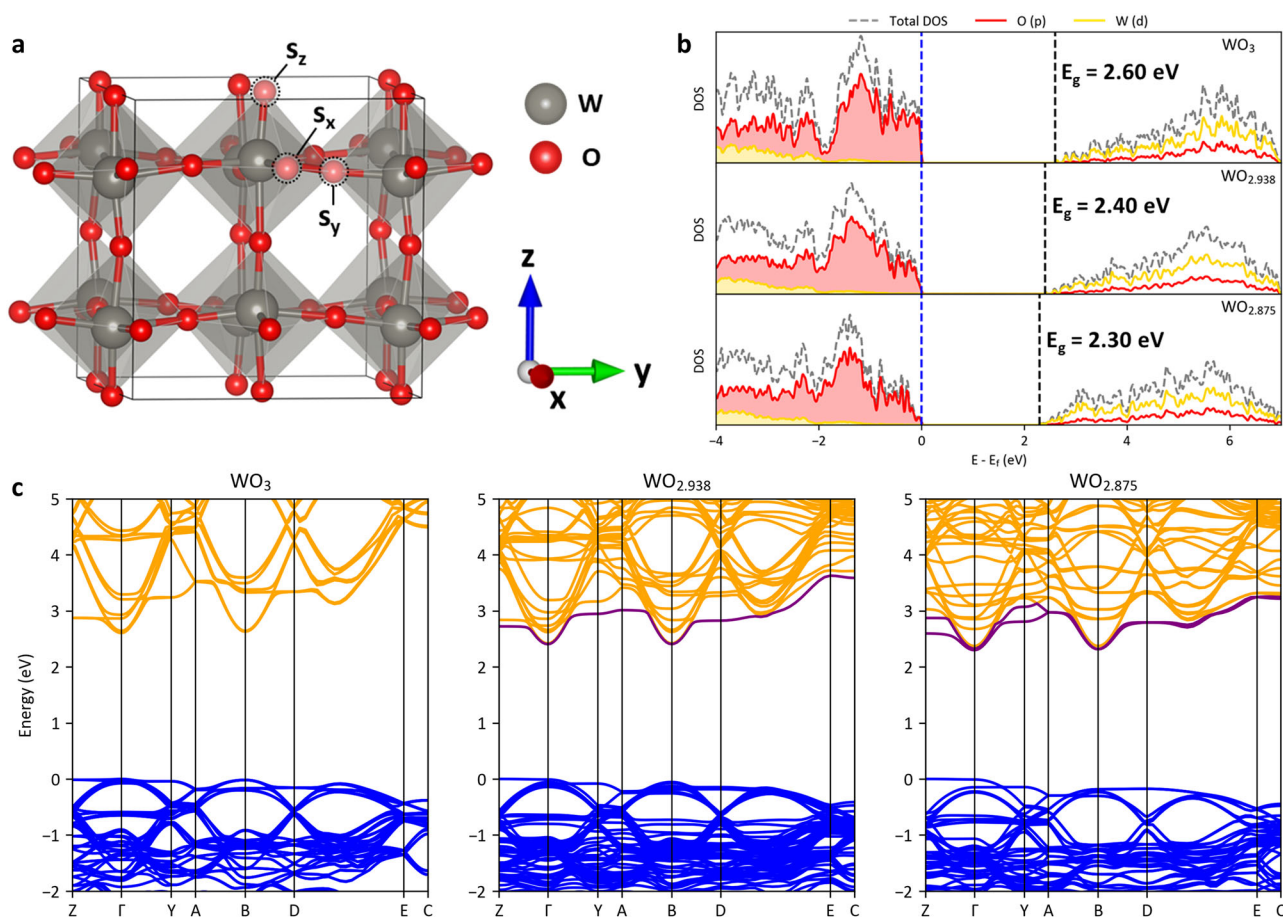


Fig. 5 | Conductance modulation mechanism based on DFT calculation. a Unit cell of the monoclinic WO₃. Non-equivalent sites of oxygen are marked as S_x, S_y, S_z. **b** Density of states (DOS) plots for WO₃ (upper), WO_{2.938} (middle), WO_{2.875} (lower). The blue dotted line corresponds to the Fermi level (E_f) energy and the black dotted line indicates the energy difference (E - E_f) equal to the CBM level. **c** Electronic band

structures of WO₃ (left), WO_{2.938} (middle), WO_{2.875} (right). The zero-energy level is aligned with the highest occupied state. Bands above the CBM and below valence band maximum (VBM) are represented by yellow and blue lines. The newly generated state by defects is highlighted in purple.

increases in device conductivity were accompanied by rises in both mobility and carrier density. These observations were corroborated by density functional theory calculations, which showed that introducing oxygen vacancies in the WO_{3-x} channel leads to the formation of defect states just below the CBM. These defect states create shallow donor levels that enhance carrier density. Additionally, the formation of oxygen vacancies is linked to structural changes around tungsten atoms, fostering the development of large polarons which are expected to boost carrier mobility.

Further distinguishing ECRAM from conventional NVM devices is its reliance on electrochemical ion transport rather than simply overcoming intrinsic stochasticity. This characteristic not only enhances reproducibility and stability in the switching process but also addresses key constraints such as scalability and random fluctuations in resistive states. Consequently, ECRAM shows significant promise for improving performance in AI accelerators and other advanced computing architectures.

Our detailed analysis also reveals that oxygen vacancies do more than mediate resistive switching; they significantly affect conductivity modulation and long-term retention under conditions. In the amorphous tungsten oxide channel, the influence of oxygen vacancies varies markedly depending on the applied gate voltage, highlighting the need for more refined modeling. Although our initial approach assumed that all oxygen vacancies carry a 2+ charge, we acknowledge that local electronic environments, temperature, and structural factors can induce different charge states. This variability can strongly impact

carrier density, and we plan to incorporate these considerations into future work. Such refinements offer a broader perspective on how material-specific ion dynamics govern device behavior, extending beyond conventional studies that may overlook the complexities of amorphous materials.

This deeper understanding of oxygen vacancies substantially aids in optimizing resistive processing units for AI accelerators, ensuring our findings constitute more than a reiteration of existing theories. Notably, our work furnishes the experimental validation of oxygen donor levels in amorphous tungsten oxide, a point previously proposed yet not empirically verified, thus laying a foundation for further developments in the field. By advancing comprehension of how oxygen vacancies dictate electron transport properties, our research stands to guide the design of more reliable and efficient ECRAM devices.

In conclusion, our study confirmed the topotactic transformation of our device through comprehensive electronic and atomic structure analysis, ensuring consistent cycle-to-cycle performance and robust endurance. This research provides crucial insight into the switching characteristics needed to meet AI computation demands. Additionally, our findings extend the understanding of oxygen vacancies as more than just drivers of resistive switching but as crucial contributors to enhancing carrier mobility and density, thus optimizing device performance under varying operational conditions which are critical for AI applications. Ultimately, the deeper mechanistic understanding gained from this study is expected to further reduce the technology

gap, accelerating the realization of robust, high-performance ECRAM solutions for AI computing.

Methods

Device fabrication

The substrate is a silicon wafer with a SiO₂ layer thickness of 100 nm. Standard photolithography and RF sputtering were used in device fabrication. Specifically, a channel with dimensions of 20 μm in width and 260 μm in length was patterned between the source and drain electrodes. This channel was subsequently filled with a 4.5 nm thick layer of WO₃, deposited via RF sputtering using an Ar flow rate of 30 sccm at 5 mTorr pressure. Following this, the W source and drain electrodes were defined using the same method. Subsequently, HfO₂ (28 nm) and W (35 nm) layers were sequentially deposited to form the gate stack, which partially covered the central region of the channel.

Electrical measurements

Throughout the experiments conducted at ambient air form measurements at 300 K, all probes were initially connected to the pads of the device under test. One probe was connected to the source electrode, another to the drain electrode, and the remaining one to the gate electrode. For both switching (potentiation and depression) and retention measurements, all probes were linked to the Keithley 2636B Source Measurement Unit (SMU). The experimental sequence was coordinated by an in-house Python package to guarantee accurate control and effective data collecting. The SMU was used to effectively ground the source electrode during pulse modulation, and +0.01 V was applied to the drain electrode for V_{ds} .

Preparation of ECRAM Hall samples

Samples for PDL variable-temperature Hall measurements were prepared, which involved patterning the material into a six-terminal Hall bar structure on an insulating substrate, depositing contacts, and installing pins. The procedure was as follows. Firstly, the wafer containing ECRAM devices fabricated into six-terminal Hall bar structures was sliced into pieces smaller than 1 \times 1 cm². Next, the sample was attached to a PCB board, and Pads for R_{xx} and R_{xy} , source drain, and gate electrodes were connected to external pads using wire bonding. Then, a temperature diode was attached near the sample with varnish, and pins were soldered.

Variable-temperature Hall measurement

The experiment setup was conducted inside a cryostat for low-temperature measurements. All measurements were carried out under vacuum conditions of 1 mTorr or lower. The sample was positioned at the center between the PDL magnets. The electronic instrumentation comprised a custom-built PDL motor control box, Keithley 2450 SMU for applying the voltage source to the sample, Keithley 2001 digital multimeter (DMM) for voltage measurement, and Keithley 7065 Hall switching matrix card equipped with high impedance buffer amplifiers for routing signals between the samples, SMU, and DMM. DC voltage source mode was utilized with V_{ds} set at 0.1 V. The PDL master magnet was rotated by a stepper motor system, typically operating at a speed of 0.75 rpm, to generate an AC field. A typical magnetic field amplitude applied to the sample was approximately 0.6 T for a PDL magnet gap of around 10 mm.

Computational details

The Vienna Ab initio Simulation Package (VASP) served as the computational framework for all density functional theory (DFT) calculations conducted in this study⁵⁰. Electron-ion interactions were modeled using the plane-wave projector augmented wave method⁵¹. Exchange-correlation effects were treated within the framework of the Perdew–Burke–Ernzerhof for solids (PBEsol) functional⁵². The plane wave cutoff energy was consistently set to 520 eV across all

calculations. The geometrically optimized lattice parameters of the monoclinic WO₃ are determined to be $a = 7.46 \text{ \AA}$, $b = 7.60 \text{ \AA}$, $c = 7.73 \text{ \AA}$, $\beta = 90.2^\circ$, closely match experimental parameters, exhibiting a deviation of less than 2%⁵³. The Brillouin zone was sampled using a $4 \times 4 \times 4$ Monkhorst-pack k -point grid for unit cell calculations and $4 \times 4 \times 2$ Monkhorst-pack k -point grid for $(1 \times 1 \times 2)$ supercell calculations. To ensure accurate results, structural relaxation was performed until both energy and forces met convergence criteria, set at 10^{-6} eV for energy and 0.01 eV \AA^{-1} for the forces acting on the atoms. For HSE06 calculations, atomic coordinates are fixed to the geometrically optimized positions obtained from PBEsol. We opted for a 28% intermixing of Hartree-Fock exact exchange, slightly deviating from the default value of 25%, because it matches well with the experimental value of WO₃ band gap.

Simulation details

To assess the impact of cycle-to-cycle variation on neural network training, we employed linear regression using a SGD algorithm to simulate pattern recognition accuracy with the MNIST dataset. Supplementary Fig. 12b displays the results of evaluating recognition accuracy (error rate). The neural network used in the simulation is a multilayer perceptron, comprising input, first hidden, second hidden, and output layers with 784, 256, 128, and 10 neurons, respectively. The 784 input neurons represent 28×28 MNIST image data, while the 10 output neurons represent digits from 0 to 9. Weight updates were executed with a learning rate of 0.01, a batch size of 1, and 30 epochs.

The evaluation of recognition accuracy revealed ideal synaptic characteristics, achieving 98.02% accuracy in the ideal scenario (0% variation). However, as cycle-to-cycle variation increased, accuracy decreased slightly to 97.8% and 96.13% at 2.5% and 5% variation, respectively. Accuracy dropped significantly to 88.31% at 7.5% and 70.63% at 10% variation. Notably, ECRAM demonstrates minimal cycle-to-cycle variation between 0% and 2.5%, making it a promising candidate for AI accelerators with high neural network training accuracy.

Data availability

The source data generated in this study are provided in the Source Data file. Source data are provided with this paper.

Code availability

Custom codes for data analysis were written in MATLAB and Python and are available from the corresponding author upon request.

References

1. Vaswani, A. et al. Attention is all you need. In *Adv. Neural Inf. Process. Syst.* 30 (eds Guyon, I. et al.) 5998–6008 (Curran Associates, Inc., 2017).
2. Chan, W. et al. Speechstew: simply mix all available speech recognition data to train one large neural network. Preprint at *arXiv preprint arXiv:2104.02133*, (2021).
3. Ambrogio, S. et al. An analog-AI chip for energy-efficient speech recognition and transcription. *Nature* **620**, 768–775 (2023).
4. Zhang, W. et al. Edge learning using a fully integrated neuro-inspired memristor chip. *Science* **381**, 1205–1211 (2023).
5. Haensch, W. et al. Compute in-memory with non-volatile elements for neural networks: a review from a co-design perspective. *Adv. Mater.* **35**, 2204944 (2023).
6. Rasch, M. J. et al. Hardware-aware training for large-scale and diverse deep learning inference workloads using in-memory computing-based accelerators. *Nat. Commun.* **14**, 5282 (2023).
7. Song, W. et al. Programming memristor arrays with arbitrarily high precision for analog computing. *Science* **383**, 903–910 (2024).
8. Le Gallo, M. et al. A 64-core mixed-signal in-memory compute chip based on phase-change memory for deep neural network inference. *Nat. Electron.* **6**, 680–693 (2023).

9. Kim, S. et al. Metal-oxide based, CMOS-compatible ECRAM for deep learning accelerator. In *2019 IEEE International Electron Devices Meeting (IEDM)* 35.7.1–35.7.4 (IEEE, 2019).
10. Tang, J. et al. ECRAM as scalable synaptic cell for high-speed, low-power neuromorphic computing. In *2018 IEEE International Electron Devices Meeting (IEDM)* 13.1.1–13.1.4 (IEEE, 2018).
11. Miyake, K., Kaneko, H. & Teramoto, Y. Electrical and optical properties of reactively sputtered tungsten oxide films. *J. Appl. Phys.* **53**, 1511–1515 (1982).
12. Jeong, Y. et al. Elucidating ionic programming dynamics of metal-oxide electrochemical memory for neuromorphic computing. *Adv. Electron. Mater.* **7**, 2100185 (2021).
13. Lee, C. et al. $\text{Pr}_{0.7}\text{Ca}_{0.3}\text{MnO}_3$ -based three-terminal synapse for neuromorphic computing. *IEEE Electron Device Lett.* **41**, 1500–1503 (2020).
14. Li, Y., Fuller, E. J. & Talin, A. A. *Redox Transistors Based on TiO_2 for Analogue Neuromorphic Computing*. (Sandia National Lab.(SNL-CA), Livermore, CA (United States), 2020).
15. Guo, Y. & Robertson, J. Origin of the high work function and high conductivity of MoO_3 . *Appl. Phys. Lett.* **105**, 222110 (2014).
16. Kim, H.-S. et al. Oxygen vacancies enhance pseudocapacitive charge storage properties of $\text{MoO}_3\text{-x}$. *Nat. Mater.* **16**, 454–460 (2017).
17. Um, M. et al. An ECRAM-based analog compute-in-memory neuromorphic system with high-precision current readout. In *Proc. 2023 IEEE Biomedical Circuits and Systems Conf. (BioCAS)* 1–5 (IEEE, 2023).
18. Li, Y. et al. In situ parallel training of analog neural network using electrochemical random-access memory. *Front. Neurosci. (Online)* **15**, 636127 (2021).
19. Chen, P. et al. Open-loop analog programmable electrochemical memory array. *Nat. Commun.* **14**, 6184 (2023).
20. Kim, S., Son, J., Kwak, H. & Kim, S. Accurate weight update in an electrochemical random-access memory based cross-point array using channel-high half-bias scheme for deep learning accelerator. *Adv. Electron. Mater.* **9**, 2300476 (2023).
21. Waser, R. & Aono, M. Nanoionics-based resistive switching memories. *Nat. Mater.* **6**, 833–840 (2007).
22. Nikam, R. D., Kwak, M. & Hwang, H. All-solid-state oxygen ion electrochemical random-access memory for neuromorphic computing. *Adv. Electron. Mater.* **7**, 2100142 (2021).
23. Gunawan, O. et al. Carrier-resolved photo-Hall effect. *Nature* **575**, 151–155 (2019).
24. Gunawan, O., Virgus, Y. & Tai, K. F. A parallel dipole line system. *Appl. Phys. Lett.* **106**, 062407 (2015).
25. Gunawan, O. & Virgus, Y. The one-dimensional camelback potential in the parallel dipole line trap: Stability conditions and finite size effect. *J. Appl. Phys.* **121**, 133902 (2017).
26. Hu, M. et al. Dot-product engine for neuromorphic computing: programming 1T1M crossbar to accelerate matrix-vector multiplication. In *Proc. 53rd Annual Design Automation Conference (DAC)*, 1–6 (IEEE, 2016).
27. Hall, E. H. On a new action of the magnet on electric currents. *Am. J. Math.* **2**, 287–292 (1879).
28. Widiyandari, H., Firdaus, I., Kadarisman, V. G. S. & Purwanto, A. Optical properties and photocatalytic activities of tungsten oxide (WO_3) with platinum co-catalyst addition. In *AIP Conference Proceedings*. **1712**, 050027 (AIP Publishing, 2016).
29. Vemuri, R., Engelhard, M. H. & Ramana, C. Correlation between surface chemistry, density, and band gap in nanocrystalline WO_3 thin films. *ACS Appl. Mater. Interfaces* **4**, 1371–1377 (2012).
30. Lim, E. W. & Ismail, R. Conduction mechanism of valence change resistive switching memory: a survey. *Electronics* **4**, 586–613 (2015).
31. Mott, N. F. & Davis, E. A. *Electronic Processes in Non-Crystalline Materials*. (Oxford University Press Oxford, 1971).
32. Nagaoka, A., Miyake, H., Taniyama, T., Kakimoto, K. & Yoshino, K. Correlation between intrinsic defects and electrical properties in the high-quality $\text{Cu}_2\text{ZnSnS}_4$ single crystal. *Appl. Phys. Lett.* **103**, 112107 (2013).
33. Le, H. M., Vu, N. H. & Phan, B.-T. Migrations of oxygen vacancy in tungsten oxide (WO_3): a density functional theory study. *Comput. Mater. Sci.* **90**, 171–176 (2014).
34. Lee K. et al. 3D stackable vertical-sensing electrochemical random-access memory using ion-permeable WS_2 electrode for high-density neuromorphic systems. *Adv. Funct. Mater.* **34**, 2313802 (2024).
35. Lee, J., Lim, S., Kwak, M., Song, J. & Hwang, H. Understanding of proton induced synaptic behaviors in three-terminal synapse device for neuromorphic systems. *Nanotechnology* **30**, 255202 (2019).
36. Zhu, L. Q., Sun, J., Wu, G. D., Zhang, H. L. & Wan, Q. Self-assembled dual in-plane gate thin-film transistors gated by nanogranular SiO_2 proton conductors for logic applications. *Nanoscale* **5**, 1980 (2013).
37. Chen, P.-Y., Peng, X. & Yu, S. NeuroSim: a circuit-level macro model for benchmarking neuro-inspired architectures in online learning. *IEEE Trans. Comput.-Aided Des. Integr. Circuits Syst.* **37**, 3067–3080 (2018).
38. Gokmen, T. & Vlasov, Y. Acceleration of deep neural network training with resistive cross-point devices: design considerations. *Front. Neurosci.* **10**, 333 (2016).
39. Kwak, H., Lee, C., Lee, C., Noh, K. & Kim, S. Experimental measurement of ungated channel region conductance in a multi-terminal, metal oxide-based ECRAM. *Semiconduct. Sci. Technol.* **36**, 114002 (2021).
40. Krukau, A. V., Vydrov, O. A., Izmaylov, A. F. & Scuseria, G. E. Influence of the exchange screening parameter on the performance of screened hybrid functionals. *J. Chem. Phys.* **125**, 224106 (2006).
41. Niklasson, G. A., Berggren, L. & Larsson, A.-L. Electrochromic tungsten oxide: the role of defects. *Sol. Energy Mater. Sol. Cells* **84**, 315–328 (2004).
42. Keith, J. B., Wang, H., Fultz, B. & Lewis, J. P. Ab initio free energy of vacancy formation and mass-action kinetics in vis-active TiO_2 . *J. Phys.: Condens. Matter* **20**, 022202 (2007).
43. Koffyberg, F.-P., Dwight, K. & Wold, A. Interband transitions of semiconducting oxides determined from photoelectrolysis spectra. *Solid State Commun.* **30**, 433–437 (1979).
44. Zimmermann, R. et al. Electronic structure of 3d-transition-metal oxides: on-site Coulomb repulsion versus covalency. *J. Phys.: Condens. Matter* **11**, 1657 (1999).
45. Aubrey, M. L. et al. Electron delocalization and charge mobility as a function of reduction in a metal–organic framework. *Nat. Mater.* **17**, 625–632 (2018).
46. Yao, X. et al. Protonic solid-state electrochemical synapse for physical neural networks. *Nat. Commun.* **11**, 3134 (2020).
47. Onen, M. et al. Nanosecond protonic programmable resistors for analog deep learning. *Science* **377**, 539–543 (2022).
48. Hasegawa, T., Tsuruoka, T., Itoh, Y., Sakamoto, T. & Aono, M. *Development of Three-Terminal Atomic Switches and Related Topics*. (Springer International Publishing, 2020).
49. Terabe, K., Tsuchiya, T., Yang, R. & Aono, M. Nanoionic devices enabling a multitude of new features. *Nanoscale* **8**, 13873–13879 (2016).
50. Kresse, G. & Furthmüller, J. Efficient iterative schemes for ab initio total-energy calculations using a plane-wave basis set. *Phys. Rev. B* **54**, 11169 (1996).
51. Blöchl, P. E. Projector augmented-wave method. *Phys. Rev. B* **50**, 17953 (1994).
52. Perdew, J. P. et al. Restoring the density-gradient expansion for exchange in solids and surfaces. *Phys. Rev. Lett.* **100**, 136406 (2008).

53. Loopstra, B. & Rietveld, H. Further refinement of the structure of WO_3 . *Acta Crystallogr. Sect. B: Struct. Crystallogr. Cryst. Chem.* **25**, 1420–1421 (1969).

Acknowledgements

This work was supported by K-CHIPS (Korea Collaborative & High-tech Initiative for Prospective Semiconductor Research) (2410000230, 20024796, 23011-15TC, and 2410000283, 20024760, 23008-45FC) funded by the Ministry of Trade, Industry & Energy (MOTIE, Korea).

Author contributions

S.K. and O.G. designed, initiated, and supervised the project. H.K. designed, fabricated, and measured the device, with help from J.C., S.H., and J.L. Hall measurement was performed by H.K., with help from J.C., C.K., P.S., B.S., and O.G. E.K. conducted the first-principle calculations, with help from D.L. All authors discussed the results. D.K. performed neural network simulation. H.K., J.C., E.K., B.S., D.L., O.G. and S.K. wrote the paper.

Competing interests

The authors declare no competing interests.

Additional information

Supplementary information The online version contains supplementary material available at <https://doi.org/10.1038/s41467-025-58004-0>.

Correspondence and requests for materials should be addressed to Oki Gunawan or Seyoung Kim.

Peer review information *Nature Communications* thanks Gang Pan, Albert Talin and Ilia Valov for their contribution to the peer review of this work. A peer review file is available.

Reprints and permissions information is available at <http://www.nature.com/reprints>

Publisher's note Springer Nature remains neutral with regard to jurisdictional claims in published maps and institutional affiliations.

Open Access This article is licensed under a Creative Commons Attribution-NonCommercial-NoDerivatives 4.0 International License, which permits any non-commercial use, sharing, distribution and reproduction in any medium or format, as long as you give appropriate credit to the original author(s) and the source, provide a link to the Creative Commons licence, and indicate if you modified the licensed material. You do not have permission under this licence to share adapted material derived from this article or parts of it. The images or other third party material in this article are included in the article's Creative Commons licence, unless indicated otherwise in a credit line to the material. If material is not included in the article's Creative Commons licence and your intended use is not permitted by statutory regulation or exceeds the permitted use, you will need to obtain permission directly from the copyright holder. To view a copy of this licence, visit <http://creativecommons.org/licenses/by-nc-nd/4.0/>.

© The Author(s) 2025